École Polytechnique Fédérale de Lausanne

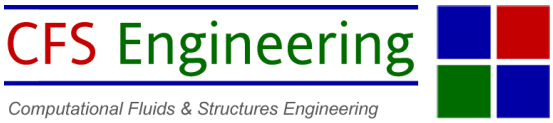

Development of the AeroFrame module in CEASIOMpy

Mechanical Engineering - Master Thesis, 2024

Romain Gauthier

Company supervisor: Dr. Jan B. Vos

Academic supervisor: Prof. François Gallaire

Acknowledgements

I would like to thank Dr. Jan Vos for the opportunity to work at CFS Engineering for my Master Thesis. This experience allowed me to explore and apply Computational Fluid Dynamics in various collaborative projects. I want to extend my thanks to Giacomo Benedetti (CFS Engineering) for his help, advice, and feedback throughout the project. I am also grateful to Alain Gehri (CFS Engineering) for sharing with me his expertise in the field of mesh generation, CFD computations, and post-processing tasks. I want to thank Jesper Oppelstrup from KTH Royal Institute of Technology in Stockholm, for his help during the beginning of the project. Finally, I would like to acknowledge Prof. François Gallaire (Laboratory of Fluid Mechanics and Instabilities, EPFL) for agreeing to supervise the project.
The work carried out in this thesis is part of the Colossus project (Collaborative System of Systems Exploration of Aviation Products, Services & Business models) funded by the European Union under Grant Agreement no. 101097120. The Swiss participation in the Colossus project is supported by the Swiss State Secretariat for Education, Research and Innovation (SERI) under contract number 22.00609.

Abstract

In classical fluid mechanics, solid structures are often treated as rigid boundaries that do not interact with fluid flow. However, many engineering applications require consideration of both aerodynamic performance and structural response, leading to the study of aeroelasticity. Aeroelasticity examines the interaction between aerodynamic forces acting upon non-rigid (deformable) structures and the resulting structural deformations. This research aims to integrate a low-fidelity aeroelastic module into the open-source aircraft design tool, CEASIOMpy, as part of the Horizon Europe project Colossus. The developed module, AeroFrame, combines a finite element method (FEM) implementation of linear beam equations for structural calculations with the vortex lattice method (VLM) for aerodynamic computations. AeroFrame is limited to static aeroelastic analyses. A partitioned approach is employed, using separate solvers for fluid and structural computations. The module maps the aerodynamic forces and the structural displacements between the two non-matching meshes (fluid and structural meshes) using nearest neighbor interpolation. Validation of AeroFrame shows consistent results for deflections smaller than around 2% of the semi-span length, aligning well with literature data and medium- to high-fidelity computations. Tests on simple rectangular wings and complex aircraft wing geometries demonstrate its capability to handle various configurations, including different cross-sections, sweep angles, and dihedral angles. While AeroFrame provides accurate results in small deformation scenarios, its estimations for large displacements differ from the solutions obtained with nonlinear shell models. AeroFrame is well-suited for preliminary aircraft design tasks, enabling extensive iterative analyses across various material properties and wing geometries due to its low computational cost.

Contents

Acronyms

AIC Aerodynamic Influence Coefficient. 4

AVL Athena Vortex Lattice. 7, 8, 10, 23

CFD Computational Fluid Dynamics. 1, 12, 16–18, 20

CPACS Common Parametric Aircraft Configuration Schema. 1, 7, 8, 10, 11, 23

CSM Computational Structural Mechanics. 16, 17, 20

DLR German Aerospace Center. 1, 7

DOF Degree Of Freedom. 10, 11

FEM Finite Element Method. 1, 5, 10, 11, 13, 14, II

FramAT Frame Analysis Tool. 10, 23

FSCON Fluid-Structure CONnector. 16

FSI Fluid-Structure Interaction. 1, 12

HARWs High Aspect Ratio Wings. 1

ICAO International Civil Aviation Organization. 10

NASTRAN NAsa STRuctural ANalysis. 14–16

NSMB Navier-Stokes Multi Block. 16, 18, 20

UID Unique Identifier. 10, 11

UNSI Unsteady Viscous Flow in the Context of Fluid-Structure Interaction. 20

VLM Vortex Lattice Method. 1–4, 11, 12, 14–16, 18, 20, II

XML Extensible Markup Language. 7

1 Introduction

In classical fluid mechanics, the solid structure is treated merely as an infinitely rigid boundary that does not interact with the fluid flow. In real engineering applications, both aerodynamic performance and structural response have to be considered. This necessity leads to the study of the interaction between aerodynamics and structural mechanics, known as aeroelasticity. Aeroelasticity is an interdisciplinary field of study that focuses on the interaction between aerodynamic and elastic forces, occurring when a non-rigid body is exposed to fluid flow. The aerodynamic forces that act on the non-rigid structures lead to structural deformations, and these structural deformations affect the aerodynamic forces. Aeroelasticity is a subfield of fluid-structure interaction (FSI). Aeroelastic phenomena are critical in the design and analysis of aircraft, bridges, and other structures subjected to aerodynamic loading, as they can significantly impact the structural integrity and performance.

The aerospace industry is looking for safer, more eco-friendly technologies while also aiming to reduce costs. This shift demands a new approach to aircraft design, with a focus on enhancing overall operational efficiency [1]. This induces a need for weight reduction and increased structural efficiency, leading to the adoption of composite thin-walled beam structures [2]. Improving aerodynamics and reducing drag can be achieved by increasing the aspect ratio of wings. There is a growing interest in high-aspect-ratio wings (HARWs) for use in transport aircraft, as they improve the lift to drag ratio. Increasing the aspect ratio effectively reduces the induced drag due to the downwash component generated by wingtip vortices. Indeed, a longer span helps mitigate the three-dimensional effects of the wing geometry on the flow. Designing wings with very high aspect ratios while maintaining sufficient structural strength is challenging. As a result, the aspect ratio of a conventional aircraft represents a compromise between competing aerodynamic and structural demands [1, 3, 4]. High-aspect-ratio wings are more flexible and undergo larger deformations that can lead to structural failure. This issue needs to be addressed in the aeroelastic design of the wing and drive the research and development of innovative computational tools for efficient and precise aeroelastic analysis [5].

The objective of this work is to integrate a static aeroelastic module in the open source conceptual aircraft design environment CEASIOMpy, in the framework of the European project Colossus. CEASIOMpy is a versatile tool for creating complex design and optimization workflows for both conventional and unconventional aircraft configurations. It is maintained by CFS Engineering in Switzerland, and Airinnova in Sweden. It offers a range of tools for various aircraft design disciplines, with its aerodynamic modules being the most advanced. These tools facilitate the automatic generation of aerodynamic meshes and computational fluid dynamics (CFD) calculations. CEASIOMpy is mostly written in `Python` and is based on the Common Parametric Aircraft Configuration Schema (CPACS) [6], a data definition for the air transportation system developed by the German Aerospace Center DLR, facilitating information exchange among engineering tools. Its central model approach minimizes the number of interfaces.

Typical existing numerical aeroelastic solvers integrate the finite element method (FEM) for structural analysis with various high-fidelity CFD models. They often yield detailed outcomes but require significant computational resources in terms of both storage and time. Their application for preliminary aircraft design is therefore not appropriate; the iterative design process, which involves altering various parameters, requires the use of faster aerodynamic models [7]. In this work, computationally simple methods are employed: a FEM beam model is paired with the vortex lattice method (VLM), which is a low-fidelity aerodynamic model. Although constrained to certain flow conditions by the VLM assumptions, this approach provides fast numerical predictions of aerodynamic loads on lifting surfaces [5]. The FEM and VLM tools are existing open-source solvers and were not developed during this project. The main goal of this work is to couple them to create the aeroelastic module.

The present report is structured as follows. A theoretical review of aeroelasticity, vortex lattice method, and beam theory is presented in section 2. The implementation of both fluid and structural models, as well as the aeroelastic coupling, are explained in section 3. The results and limitations are discussed in sections 4 and 5, respectively.

2 Theoretical background

2.1 Aeroelasticity review

Aeroelasticity includes both static and dynamic phenomena. A short overview of fluid-structure interaction engineering issues is given in the following subsections. A detailed description can be found in *Aircraft Stuctures for Engineering Students* by T.H.G. Megson [8]. In this work, only static aeroelastic calculations are considered.

2.1.1 Static aeroelasticity

Static aeroelasticity involves the interaction between aerodynamic forces and structural deformation under steady-state conditions, during cruise for instance. If the rigidity of the wing is high enough, an equilibrium between aerodynamic loads and elastic forces can be reached, leading to a stable configuration of the wing. In the case of a too flexible structure, instability such as divergence can occur; the aerodynamic loads induce a twist of the wing around the span axis, leading to an increase in forces and creating a feedback loop until structural failure. Another static aeroelastic problem is control reversal; the elastic deformation of the structure can alter (or reverse) the expected influence of control surfaces like ailerons, elevators, and rudders. It affects the aircraft's stability as the pilot cannot control the aircraft in the usual way. Both divergence and control reversal can be prevented by performing static aeroelastic computations during the wing design.

2.1.2 Dynamic aeroelasticity

Dynamic aeroelasticity deals with the interaction between unsteady aerodynamic forces and structural response. It often leads to complex oscillatory behavior, influenced by both elastic and dynamic properties of the wing. Flutter is a dynamic instability, characterized by a coupling between the energy from aerodynamic loads and oscillatory modes of the structure. Wings must be carefully designed to avoid flutter phenomena, which can lead to rapid structural failure. Dynamic analyses require more advanced numerical tools and significantly greater computational time; these are not covered in this work.

2.2 Vortex lattice method (VLM)

The aerodynamic loads used for the aeroelastic calculations are computed using the vortex lattice method (VLM), which is a low-fidelity numerical model generally used in the initial phases of aircraft design. It can be applied to 3-dimensional aerodynamic configurations composed of thin lifting surfaces with small angles of attack and sideslip. The following theoretical review is mainly based on the textbooks *Flight Vehicle Aerodynamics* by M. Drela [9], *Low-Speed Aerodynamics* by J. Katz and A. Plotkin [10], and *Aerodynamics for Engineers* by Bertin and Smith [11].

2.2.1 Assumptions of the VLM

The VLM is built on the quasi-steady ideal flow theory, also known as potential flow. This assumes incompressible, irrotational, and inviscid flow. However, VLM solvers usually employ

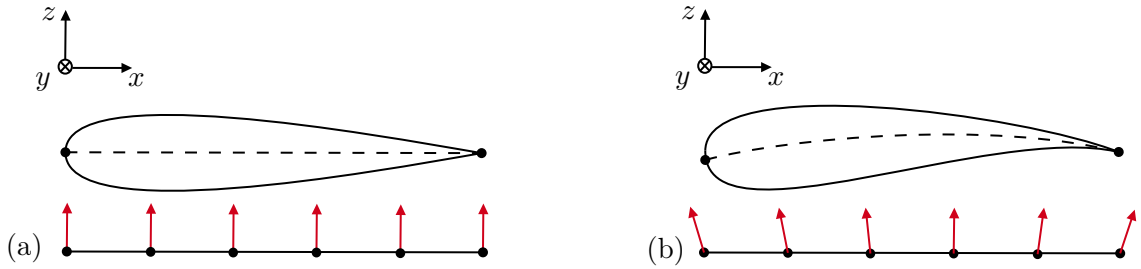

Figure 1 – Definition of the normal vector of the lifting surface, for (a) a symmetric airfoil with no camber, and (b) a non-symmetric airfoil with positive camber (figure adapted from [12]).

the classical Prandtl-Glauert transformation to rescale the incompressible equations, using the factor

$$\eta = \sqrt{1 - M_\infty^2}, \tag{2.1}$$

with M_∞ being the upstream Mach number. This transformation allows to perform computations with a Mach number up to 0.6. The VLM assumes thin lifting surfaces and neglects the thickness of the wing in the computations of the aerodynamic forces. The camber line of the airfoil profile can be taken into account by the orientation of the normal vector of the wing surface (fig. 1). Another assumption is that the angle of attack and the angle of sideslip are both small, as flow separation cannot be modeled. Since the flow is ideal, viscous effects are neglected, as well as turbulence and boundary layer phenomena. Only lift-induced drag can be computed.

2.2.2 Equations of the VLM

The assumption of irrotational flow leads to the existence of a potential scalar variable, called velocity potential [10]. The total flow velocity at each point is given by its gradient:

$$\boldsymbol{V} = \nabla(\Phi_\infty + \phi), \tag{2.2}$$

where Φ_∞ is the upstream velocity potential and ϕ is the perturbation velocity potential. Combining eq. (2.2) with the continuity equation for incompressible flow, i.e. $\nabla \cdot \boldsymbol{V} = 0$, leads to the following linear partial differential equation

$$\nabla^2(\Phi_\infty + \phi) = 0, \tag{2.3}$$

called Laplace equation. The latter second order equation requires two boundary conditions to be solved. The solutions for a flow around a wing must satisfy the flow-tangency boundary condition on the body [4]. This Neumann boundary condition on the velocity potential imposes a zero normal flow across the wing surface:

$$\nabla(\Phi_\infty + \phi) \cdot \hat{\boldsymbol{n}} = 0, \tag{2.4}$$

where $\hat{\boldsymbol{n}}$ is the surface normal vector. The second boundary condition is that the perturbation velocity must vanish in the far field:

$$\lim_{|\boldsymbol{r}| \to \infty} \nabla\phi = 0, \tag{2.5}$$

with $\boldsymbol{r} = (x, y, z)$ being the position vector. Numerically, the VLM is an implementation of the general 3-dimensional lifting surface problem, in which the flow around the wings of an aircraft configuration is modeled using vortex-sheets with a strength distribution [9]. This principle uses vortex filaments bound to a fixed location in the flow to replace the wing, called bound vortices. According to Helmholtz's theorem, a vortex filament cannot end in the fluid; therefore it must

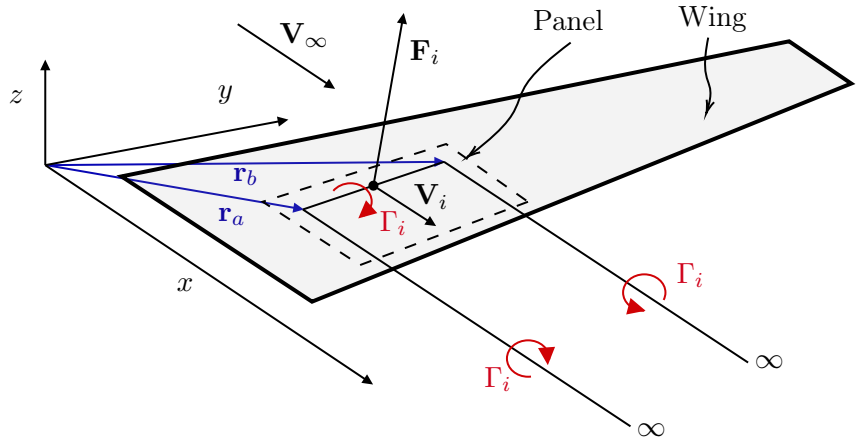

Figure 2 – Representation of one single horseshoe vortex of strength Γ_i, composed of a bound vortex located a the quarter-chord of the panel, and two trailing vortices going downstream to infinity.

continue as two free vortices trailing downstream from the bound endpoints to infinity. It leads to vortices with a horseshoe shape, called horseshoe vortices [4] (fig. 2). The VLM discretizes the vortex-sheet strength distribution by dividing the lifting surfaces into panels and uses a lattice of horseshoe vortices, each of them contributing to the flow velocity at any field point. The number of panels used depends on the required accuracy in the computation of the pressure distribution on the wing surface. The strength Γ_i of each vortex is initially unknown and must be determined as part of the solution. The bound vortex, modeling the lifting properties, is placed at the quarter chord position of the panel. The control point, at which the flow-tangency boundary condition is satisfied, is located at the center of the panel's three-quarter chord line [10, 11]. The velocity field induced by the lattice of panels at any point $\boldsymbol{r}$ can be computed by a sum of Biot-Savart line integrals [4, 9]:

$$\boldsymbol{V}(\boldsymbol{r}) = \sum_{i=1}^{N} \frac{\Gamma_i}{4\pi} \int \frac{\mathrm{d}\boldsymbol{l} \times (\boldsymbol{r} - \boldsymbol{r}')}{|\boldsymbol{r} - \boldsymbol{r}'|^3}, \tag{2.6}$$

where $\mathrm{d}\boldsymbol{l}$ is a vector along the vortex filament at position $\boldsymbol{r}'$, and N is the number of panels. The velocity $\boldsymbol{w}_{ij} \equiv \bar{\boldsymbol{w}}_{ij}\Gamma_j$ induced on the i^{th} vortex by the j^{th} vortex can be obtained, where the terms $\bar{\boldsymbol{w}}_{ij}$ form the so-called aerodynamic influence coefficient (AIC) matrix [13]. The free-stream velocity vector is defined as

$$\boldsymbol{V}_\infty = U_\infty \begin{bmatrix} \cos\alpha\cos\beta \\ -\sin\beta \\ \sin\alpha\cos\beta \end{bmatrix}, \tag{2.7}$$

where U_∞ is the free-stream speed, α is the angle of attack, and β is the angle of sidesplip. For each control point, the induced velocity contributions of every vortex associated with each panel are summed. The Neumann flow-tangency boundary condition given by eq. (2.4) has to be satisfied at each panel's control point:

$$\boldsymbol{V}_i \cdot \hat{\boldsymbol{n}}_i = \left(\boldsymbol{V}_\infty + \sum_{j=1}^{N} \bar{\boldsymbol{w}}_{ij}\Gamma_j \right) \cdot \hat{\boldsymbol{n}}_i = 0, \tag{2.8}$$

with N being the number of panels. This boundary condition problem results in the following set of linear algebraic equations:

$$\begin{bmatrix} a_{11} & a_{12} & \dots & a_{1N} \\ a_{21} & \ddots & & \vdots \\ \vdots & \ddots & & \vdots \\ a_{N1} & \dots & \dots & a_{NN} \end{bmatrix} \begin{bmatrix} \Gamma_1 \\ \Gamma_2 \\ \vdots \\ \Gamma_N \end{bmatrix} = \begin{bmatrix} b_1 \\ b_2 \\ \vdots \\ b_N \end{bmatrix}, \tag{2.9}$$

where $a_{ij} = \bar{\boldsymbol{w}}_{ij} \cdot \hat{\boldsymbol{n}}_i$ and $b_i = U_\infty[-\cos\alpha\cos\beta, \sin\beta, -\sin\alpha\cos\beta] \cdot \hat{\boldsymbol{n}}_i$. The far field boundary condition given by eq. (2.5) is directly satisfied by all the singularities considered, as the perturbation velocity obtained from the Biot-Savart law vanishes for $\boldsymbol{r} \to \infty$ [10]. The system of equations is solved for the vortex strength Γ_i, and the aerodynamic force acting on each panel is computed from the Kutta-Joukowski theorem:

$$\boldsymbol{F}_i = \rho \boldsymbol{V}_i \times \boldsymbol{l}_i \Gamma_i, \tag{2.10}$$

with ρ being the fluid density, $\boldsymbol{V}_i$ the velocity vector at the midpoint of the i^{th} bound vortex, and $\boldsymbol{l}_i = \boldsymbol{r}_b - \boldsymbol{r}_a$ (fig. 2) the bound vortex vector [9].

2.3 Classical beam theory

FEM includes in general several methods to compute the deformation of wings. In this work, the Euler-Bernoulli beam theory (also known as classical beam theory) is used. It is a simple method that provides good results in the case of high aspect ratio wings [2], which is the case of most aircraft wings. The beam model is computationally less expensive than plate or shell model and provides comparable results for static aeroelastic response and preliminary wing design [2, 14]. The differences are mainly due to the consideration of shear deformations in the shell model, that are neglected in the beam model. The following Euler-Bernoulli beam theory review is based on the textbooks *Structural Analysis* by Bauchau, Craig [15] and *Elastic Beams in Three Dimensions* by Andersen, Nielsen [16].

2.3.1 Assumptions of classical beam theory

A beam is a structure with one of its reference lengths being much larger than the other two. The longitudinal $x-$axis of the beam is defined along the longer dimension, and the cross-section belongs to the $y-z$ plane. The $x-$axis is assumed to pass through the centroid of the cross-section (centroidal axis system), and the $y-$ and $z-$axis are defined as the principal centroidal axes of bending.

A first assumption of Euler-Bernoulli beam theory is that the cross-section of the beam is infinitely rigid in its own plane. The cross-section remains plane after beam deformation, and normal to the deformed axis of the beam. The deformed position of the cross-section is uniquely defined by a position vector $\boldsymbol{u} = \boldsymbol{u}(x)$ and a rotation vector $\boldsymbol{\theta} = \boldsymbol{\theta}(x)$ with the following components:

$$\boldsymbol{u} = \begin{bmatrix} u_x \\ u_y \\ u_z \end{bmatrix}, \quad \boldsymbol{\theta} = \begin{bmatrix} \theta_x \\ \theta_y \\ \theta_z \end{bmatrix}, \tag{2.11}$$

in the (x, y, z)-coordinate system. To permit the use of linear theory, it is assumed that displacements and rotation components are small. The material is assumed isotropic and the constitutive law between stresses and strains is given by linear Hooke's law.

2.3.2 Governing equations of beam theory

The governing equations of the 3-dimensional Euler-Bernoulli beam theory can be obtained from a force and moment balance on an infinitesimal beam element loaded by external distributed forces $\boldsymbol{q} = (q_x, q_y, q_z)$ and external distributed moments $\boldsymbol{m} = (m_x, m_y, m_z)$ [12]:

$$\frac{\mathrm{d}}{\mathrm{d}x}\begin{bmatrix} F_x \\ F_y \\ F_z \end{bmatrix} + \begin{bmatrix} q_x \\ q_y \\ q_z \end{bmatrix} = \mathbf{0}, \tag{2.12a}$$

$$\frac{\mathrm{d}}{\mathrm{d}x}\begin{bmatrix} M_x \\ M_y \\ M_z \end{bmatrix} + \begin{bmatrix} m_x \\ m_y \\ m_z \end{bmatrix} + \begin{bmatrix} 0 \\ -F_z \\ F_y \end{bmatrix} = \mathbf{0}, \tag{2.12b}$$

where $\boldsymbol{F} = (F_x, F_y, F_z)$ and $\boldsymbol{M} = (M_x, M_y, M_z)$ are the internal forces and moments, respectively. In the limit of small deformations, the following relations can be obtained for axial stretching force, bending moments, and torsional moment:

$$F_x = EA\frac{\mathrm{d}u_x}{\mathrm{d}x}, \tag{2.13a}$$

$$M_z = EI_z\frac{\mathrm{d}^2u_y}{\mathrm{d}x^2}, \tag{2.13b}$$

$$M_y = -EI_y\frac{\mathrm{d}^2u_z}{\mathrm{d}x^2}, \tag{2.13c}$$

$$M_x = GJ\frac{\mathrm{d}\theta_x}{\mathrm{d}x}, \tag{2.13d}$$

where E and G are the elastic and shear moduli of the material, A is the beam cross-section area, I_y and I_z are the second moments of area of the beam cross-section, and J is the polar moment of inertia of the beam cross-section. Combining equilibrium eqs. (2.12a) and (2.12b) with eqs. (2.13a) to (2.13d) leads to the following set of governing equations:

$$\frac{\mathrm{d}}{\mathrm{d}x}\left[EA\frac{\mathrm{d}u_x}{\mathrm{d}x}\right] + q_x = 0, \tag{2.14a}$$

$$\frac{\mathrm{d}^2}{\mathrm{d}x^2}\left[EI_z\frac{\mathrm{d}^2u_y}{\mathrm{d}x^2}\right] + \frac{\mathrm{d}m_z}{\mathrm{d}x} - q_y = 0, \tag{2.14b}$$

$$\frac{\mathrm{d}^2}{\mathrm{d}x^2}\left[EI_y\frac{\mathrm{d}^2u_z}{\mathrm{d}x^2}\right] - \frac{\mathrm{d}m_y}{\mathrm{d}x} - q_z = 0, \tag{2.14c}$$

$$\frac{\mathrm{d}}{\mathrm{d}x}\left[GJ\frac{\mathrm{d}\theta_x}{\mathrm{d}x}\right] + m_x = 0. \tag{2.14d}$$

The above four ordinary differential equations are uncoupled, i.e. each of them can be solved separately. The use of the principal centroidal axis of bending decouples the axial and bending behaviors of the beam [15]. The equations are second order in the axial displacement u_x and torsional angle θ_x, and fourth order in the transverse displacements u_y and u_z. Twelve boundary conditions are needed to solve the entire set of equations. In the case of an aircraft wing, the root can be modeled as clamped at $x = 0$, leading to:

$$\boldsymbol{u}(x=0) = \mathbf{0}, \qquad \theta_x(x=0) = 0, \tag{2.15a}$$

$$u_y'(x=0) = u_z'(x=0) = 0, \tag{2.15b}$$

which imposes neither displacements nor rotations and zero displacement slopes at the wing root (the notation $[.]'$ stands for derivative with respect to x). The wing tip located at $x = L$ is

modeled as a free-end, meaning that the bending moments and the shear force are zero at the tip. It leads to the following set of boundary conditions:

$$u_x'(x = L) = 0, \qquad \theta_x'(x = L) = 0 \tag{2.16a}$$

$$u_y''(x = L) = u_z''(x = L) = 0, \tag{2.16b}$$

$$\frac{\mathrm{d}}{\mathrm{d}x}\left[EI_z \frac{\mathrm{d}^2 u_y}{\mathrm{d}x^2}\right]\Bigg|_{x=L} = \frac{\mathrm{d}}{\mathrm{d}x}\left[EI_y \frac{\mathrm{d}^2 u_z}{\mathrm{d}x^2}\right]\Bigg|_{x=L} = 0. \tag{2.16c}$$

The governing eqs. (2.14a) to (2.14d) can be solved for the displacement vector $\boldsymbol{u}$ and the torsional rotation θ_x using the above boundary conditions. Since Euler-Bernoulli theory assumes that the rotated cross-section is always orthogonal to the deformed beam axis, the rotations θ_y and θ_z can be obtained from the following kinematic relations [16]:

$$\theta_y = -\frac{\mathrm{d}u_z}{\mathrm{d}x}, \qquad \theta_z = \frac{\mathrm{d}u_y}{\mathrm{d}x}, \tag{2.17}$$

assuming small displacements and small rotations.

3 Computational model implementation

This section provides a description of the numerical tools used in the framework of the aeroelastic module, called AeroFrame, for both fluid and structural computations. The software employed for vortex lattice method implementation and finite element method beam model are presented. Finally, the implementation of the aeroelastic coupling is described.

3.1 Fluid model

The vortex lattice method is implemented using the Athena Vortex Lattice (`AVL`) solver written by M. Drela and H. Youngren. An objective of this work is to build a module based on a `CPACS` [6] format file given as input in CEASIOMpy. It has a `XML` structure and stores the definition of all components of the aircraft, such as wing section geometry, fuselage shapes, or engine data. The first step is to read the `CPACS` and extract all the information needed to build the plane geometry in `AVL`. Multiple `Python` scripts have been developed to execute this task, using the `TIXI` library [17] created by DLR, which simplifies the reading of `XML` structure as well as the data extraction.

```
1  aircraft_name
2
3  #Mach
4  0.3
5
6  #IYsym   IZsym  Zsym
7  0        0      0
8
9  #Sref    Cref   Bref
10 122.4    4.193  25.6
11
12 #Xref  Yref   Zref
13 0.0    0.0    0.0
14
```

Figure 3 – Example of the header of `AVL` geometry input file. It contains the aircraft name, the free-stream Mach number, the symmetry settings, the reference dimensions, and the default location about which moments and rotation rates are defined.

```
SURFACE
Wing

!Nchordwise  Cspace  Nspanwise  Sspace
20.0         1.0     50.0       1.0

YDUPLICATE
0

ANGLE
0.0

SCALE
1.0  1.0  1.0

TRANSLATE
12.746   0.0  -1.136

SECTION
#Xle     Yle     Zle      Chord    Ainc
0.000    1.734   0.000    6.076    2.0

AFILE
/users/.../D150_arifoil1.dat
```

Figure 4 – Example of the surface data of `AVL` input file. It defines the number of horseshoe vortices to use, some geometric parameters, and the sections of the wing. Note that only one section is shown for the sake of space.

3.1.1 Geometry input file for AVL

After reading the `CPACS` file to extract the aircraft geometry, the next step is to produce an input file `aircraft.avl` that contains the vortex lattice parameters and the aerodynamic geometry through the definition of the wing sections properties. The geometry is described in a cartesian coordinate system: the $x-$axis is oriented downstream along the aircraft fuselage axis, the $y-$axis goes along the span of the right wing, and the $z-$axis is oriented upward. Only the main parameters of the input file are presented; a full description can be found in `AVL` documentation.

Header data: The input file starts with a header containing first the aircraft name, the free-stream Mach number, and symmetry settings (fig. 3). Reference surface area S_{ref}, chord length C_{ref}, and span length B_{ref} are provided for the calculation of the aerodynamic coefficients. The default location about which moments and rotation rates are defined by X_{ref}, Y_{ref}, and Z_{ref}.

Surface data: Each lifting surface is declared with the `SURFACE` keyword, followed by the general parameters of the wing (fig. 4). The number of chordwise and spanwise vortices placed on the surface are precised (N_{chord} and N_{span}), as well as the chordwise and spanwise vortex spacing parameter (C_{space} and B_{space}). These parameters define the desired vortex lattice resolution to discretize the wing. The `YDUPLICATE` keyword creates a second surface as a geometric symmetry of the one being defined. The duplicated surface is not assumed to be an aerodynamic image, but is truly independent. Practically, defining the right wing together with `YDUPLICATE 0.0` will conveniently create the entire wing. The `SCALE` and `TRANSLATE` keywords allow convenient 3-dimensional rescaling and relocation of the entire surface. The `ANGLE` keyword is used to modify the incidence angle of the entire surface.
Once the general parameters of the lifting surface are defined, the wing is divided into multiple

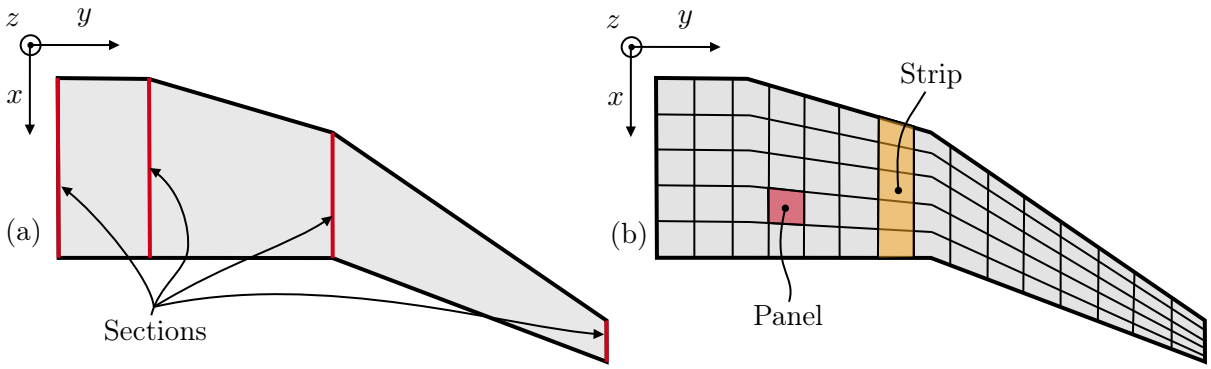

Figure 5 – Wing geometry and meshing definition: (a) the wing is defined by 4 sections along the span, and (b) discretization of the wing into 5×15 panels.

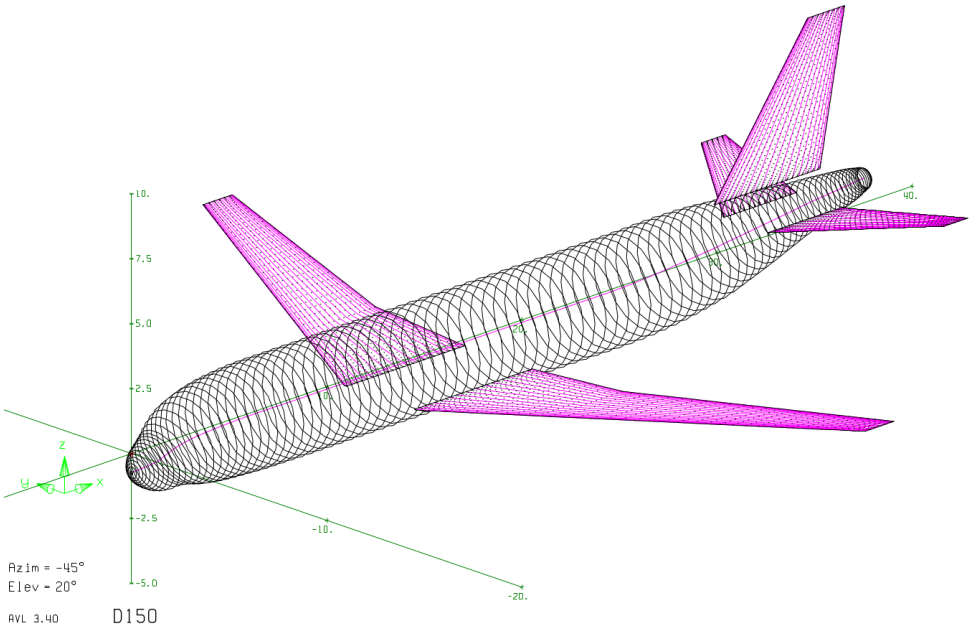

Figure 6 – Aircraft configuration in `AVL` including main wings, vertical and horizontal stabilizers, and fuselage.

sections (fig. 5). At least two of them are needed to define a wing: the root section and the tip section. The `SECTION` keyword creates an airfoil-section camber line at a spanwise location on the wing surface. Its position is defined by the leading edge location $(x_{\text{le}}, y_{\text{le}}, z_{\text{le}})$, the chord length c, and the local incidence angle. The trailing edge is located at $(x_{\text{le}} + c, y_{\text{le}}, z_{\text{le}})$, i.e. each section remains in the x-z plane. The local chord and incidence angle are linearly interpolated between the multiple sections along the span. If not specified, the airfoil camber line shape is a flat plate. The `AFILE` keyword can be used to define non-flat camber lines. The path to a file containing the airfoil points $(x/c, y/c)$ has to be provided to compute the camber line and adapt the orientation of the normal surface vector along the chord.

Body data: The `BODY` keyword can be used to define a fuselage part. It is modeled with a source and a doublet line along its longitudinal axis. The location parameters are similar to the ones described for the wing surface definition. The `BFILE` keyword allows to give the path to a file containing the side view points coordinates of the fuselage, which is assumed to have a circular cross-section. The diameter of the fuselage is computed as the difference between the

top and bottom z values for each x location along the longitudinal axis. Such a fuselage body produces no lift, but will still influence the moments. Figure 6 shows an example configuration of an aircraft definition in `AVL`, including wings and fuselage.

The first task of this project was to develop `Python` scripts to extract the aircraft geometry from the `CPACS` file and translate it to the `AVL` input file definition just described.

3.1.2 Execution of AVL and results

Once the geometry is well defined in `AVL`, the flight conditions have to be specified. In CEASIOMpy, the user provides the Mach number, the altitude, the angle of attack, and the angle of sideslip. The `ambiance` library [18] is used to compute the air density and the speed of sound from the flight altitude. This library is a full implementation of the International Civil Aviation Organization (ICAO) standard atmosphere 1993, written in `Python`. The calculation can then be executed and the system given by eq. (2.9) is solved for the strength of the vortices. Total forces, as well as loads for the individual surfaces, strips, or vortex elements are computed. In the frame of an aeroelastic analysis, the aerodynamic force applied to each panel is needed in order to properly define the load distribution on the structural model. For each panel, `AVL` provides the (x, y, z) coordinates of the bound vortex. The panel's area is computed as

$$A_p = \frac{dxW}{\cos\theta}, \tag{3.1}$$

where dx and W are respectively the panel length and width, and $\theta = -\arctan(s)$ with s being the slope of the local camber line. The local normal vector is derived from the local incidence α_p and the strip dihedral angle γ as

$$\hat{\boldsymbol{n}} = \cos\theta\frac{\boldsymbol{n_1}}{|\boldsymbol{n_1}|} + (1-\cos\theta)\hat{\boldsymbol{n}}_{\boldsymbol{2}}\left(\hat{\boldsymbol{n}}_{\boldsymbol{2}}\frac{\boldsymbol{n_1}^{\mathrm{T}}}{|\boldsymbol{n_1}|}\right) + (1-\sin\theta)\frac{\boldsymbol{n_1}}{|\boldsymbol{n_1}|}\bar{\bar{\boldsymbol{T}}}, \tag{3.2}$$

where $\boldsymbol{n_1} = \begin{bmatrix} \sin\alpha_p\cos\gamma \\ -\cos\alpha_p\sin\gamma \\ \cos\alpha_p\cos\gamma \end{bmatrix}$, $\hat{\boldsymbol{n}}_{\boldsymbol{2}} = \begin{bmatrix} 0 \\ \cos\gamma \\ \sin\gamma \end{bmatrix}$, and $\bar{\bar{\boldsymbol{T}}} = \begin{bmatrix} 0 & -\sin\gamma & \cos\gamma \\ \sin\gamma & 0 & 0 \\ -\cos\gamma & 0 & 0 \end{bmatrix}$.

The aerodynamic force $\boldsymbol{F}$ acting on each panel is finally computed as:

$$\boldsymbol{F} = qA_pC_p\hat{\boldsymbol{n}}, \tag{3.3}$$

with $q = \rho U_\infty^2/2$ being the dynamic pressure and C_p the pressure coefficient. In a few words, `AVL` computations allow to determine the resulting force for each panel element, along with its point of application on the wing.

3.2 Structural model

The structural computations are executed using Frame Analysis Tool (`FramAT`) [19], a FEM implementation of the Euler-Bernoulli linear beam theory developed during a Msc Thesis [12] at Airinnova.

3.2.1 FramAT model definition

The beam is discretized with a mesh of line segment elements. Each node is defined by its (x, y, z) coordinates and a unique identifier (UID), allowing an easy access to a specific node or range of nodes. Each node has 6 degrees of freedom (DOF): 3 for translation and 3 for rotation.

All distinct beam features have a UID, permitting properties, loads, and boundary conditions to be precisely applied. A desired number of material and cross-section features can be created, containing the material and geometric properties. This method allows for the modeling of beams with variable cross-sections along their axes. It is appropriate for the case of an aircraft wing; the cross-sectional area generally decreases from the root to the tip, and the airfoil profile may also vary along the span. The area and the second moments of inertia of each wing section are numerically computed from the points of the corresponding airfoil profile given in the `CPACS` input file. Then, the values are linearly interpolated between the sections along the span to obtain the geometric properties at each beam node. There are multiple ways of applying external aerodynamic forces to the nodes of the beam structure. Forces and moments can be applied to specific nodes, as point loads. Distributed loads (forces and moments by unit length) can be applied over a range of different nodes. The (x, y, z) components of the forces and moments (or forces and moments by unit length) have to be specified. In this study, the aerodynamic force acting on each VLM panel is applied to a beam node as a point load (the transfer of the forces to the structural mesh is discussed later). Appropriate boundary conditions must be employed to ensure the beam structure is statically determined (or isostatic) to run a static analysis. In the framework of wing deformation analysis, all DOF are fixed at the wing root.

3.2.2 Execution of FramAT and results

After the model definition, the beam governing eqs. (2.14a) to (2.14d) are solved by FEM, with a Galerkin discretization method. The solution gives the displacement vector $\boldsymbol{u}$ and the rotation vector $\boldsymbol{\theta}$ at each structural node, quantifying the wing deformation under the aerodynamic loads.

3.3 Aeroelastic coupling

3.3.1 Aeroelastic-loop

The main challenge of this work is to couple the aerodynamic loads, computed by the VLM, with the FEM model for structural deformations of the wing. The pressure distribution computed on the wing surface induces a deformation, which alters the aerodynamic load, resulting in a subsequent deformation. This iterative interaction between aerodynamic forces and structural response is modeled in an aeroelastic-loop (fig. 7). In this work a partitioned approach is used, i.e.

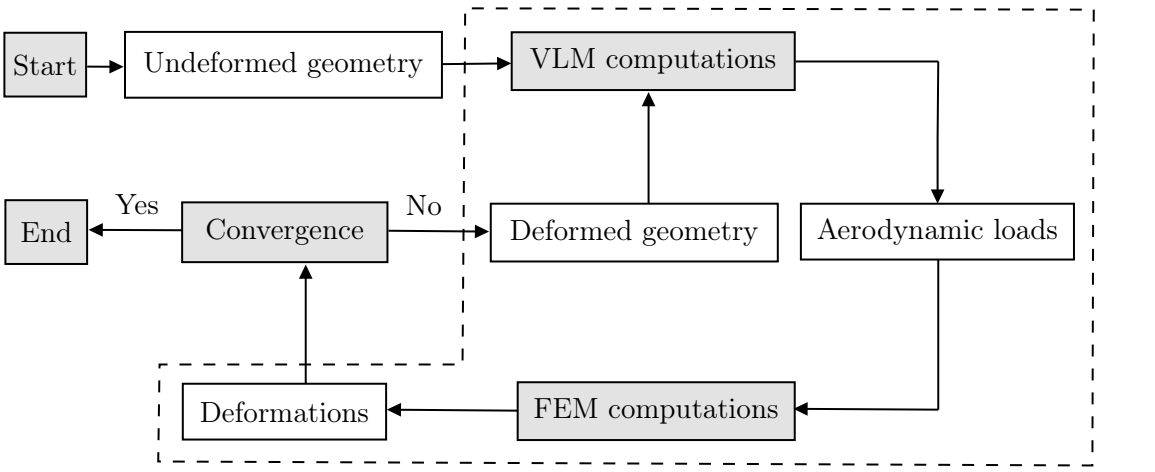

Figure 7 – Principle of the aeroelastic-loop, starting from the undeformed configuration and iterating between fluid and structural computations to find the final shape of the wing. Note that the loop stops if the maximum number of iterations is reached.

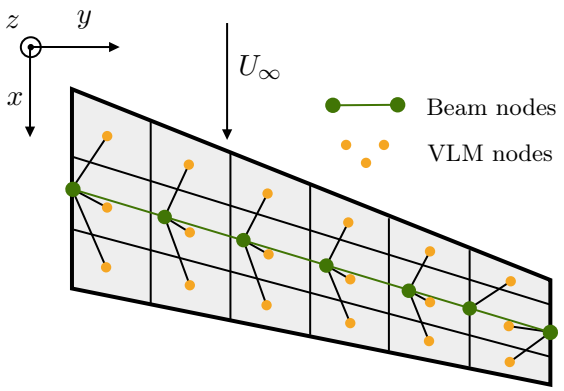

Figure 8 – Illustration of the non-matching meshes on a wing. Each VLM panel is assigned to the closest beam node (figure adapted from [12]).

separate solvers for fluid and structural computations are employed. This method contrasts with the monolithic approach, which solves a single system of coupled equations, including both fluid and structural dynamics [20]. The partitioned approach necessitates the transfer of information between fluid and structure solvers at each iteration; the aerodynamic forces are transferred to the nodes of the beam model, and the displacement of the structural nodes is transmitted to the VLM mesh. The following subsections give a description of the data transfer.

3.3.2 Coupling of VLM/FEM meshes and mapping method

The VLM discretizes the lifting surfaces into panels, resulting in a 2-dimensional mesh. On the other hand, the beam model employs a 1-dimensional mesh composed of line segment elements. During the aeroelastic-loop, the data exchange has to be done between these two non-matching meshes (fig. 8). This mismatch is usually always present in FSI analysis, as CFD computations generally require a much more refined mesh compared to structural calculations [21]. A comparison of coupling methods for information transfer between non-matching meshes in FSI computations has been done by de Boer et al. [22]. In this work, the nearest neighbor interpolation is used; each VLM panel is assigned to the closest beam node. This is the simplest and fastest method to obtain information from a mesh to another, and it ensures conservative mapping while transferring structural displacements or point loads [22, 23].

3.3.3 Work conservation and load/displacement mapping

The beam nodes are positioned at the mid-chord location along the wing span, hence most of the aerodynamic forces computed by VLM are acting with an offset from the beam axis. To account for this offset, the force is transferred from the panel to the assigned beam node, and a moment is applied to consider the distance between the original application point of the force and the projected application point. Assuming that the load is transferred via a rigid connection, the projected force together with the moment have the same contribution as the original force [12]. To ensure the aeroelastic-loop is physically meaningful, deformations and loads must be equal at the interface between fluid and structure. All aerodynamic loads have to be transmitted from the fluid to the structure, and the work done by the fluid on the panel surface has to be the same as the work done by the transferred forces on the structure [20]. Define a beam node P, and its assigned panel surface Ω on which an aerodynamic force $\boldsymbol{F}^A$ is applied (fig. 9). The resulting point loads acting on the beam structure are:

$$\boldsymbol{F}^S = \boldsymbol{F}^A, \tag{3.4a}$$

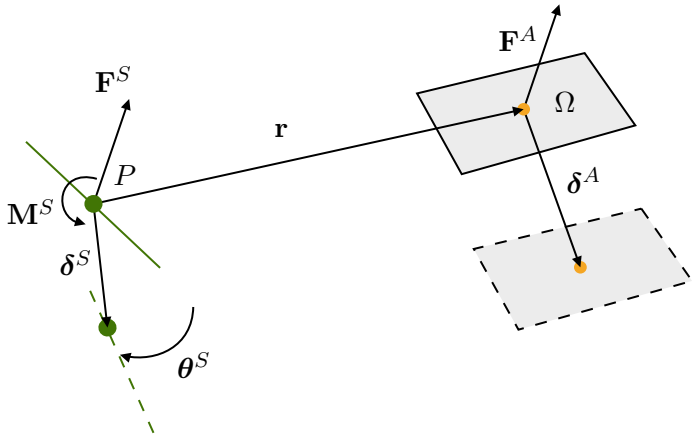

Figure 9 – Loads and displacements of a beam node P and the assigned panel element Ω. The upper-script S and A stand for structural mesh and aerodynamic mesh, respectively (figure adapted from [20]).

$$\boldsymbol{M}^S = \boldsymbol{r} \times \boldsymbol{F}^A, \tag{3.4b}$$

where $\boldsymbol{r}$ is the distance vector between the beam node P and its assigned VLM point. The displacements $\boldsymbol{\delta}^S$ and rotations $\boldsymbol{\theta}^S$ of the beam node are solved with the FEM implementation of the beam equations presented in section 2.3. The associated displacement $\boldsymbol{\delta}^A$ of the panel surface can be obtained from the work conservation principle [20]. The aerodynamic force produces a work

$$W^A = \boldsymbol{F}^A \cdot \boldsymbol{\delta}^A, \tag{3.5}$$

and the work done by the transferred loads on the structure is

$$W^S = \boldsymbol{F}^S \cdot \boldsymbol{\delta}^S + \boldsymbol{M}^S \cdot \boldsymbol{\theta}^S. \tag{3.6}$$

To ensure conservation of work, i.e. $W^S = W^A$, and from eqs. (3.4a) and (3.4b), the displacement of the panel must be

$$\boldsymbol{\delta}^A = \boldsymbol{\delta}^S + \boldsymbol{r} \times \boldsymbol{\theta}^S. \tag{3.7}$$

The displacement of the panel surface depends on both the beam node displacement and its rotation. The value of $\boldsymbol{\delta}^A$ is used to define the new position of the panel surface from its current configuration. It results in a deformed wing geometry, which is used to compute the updated aerodynamic forces to continue the aeroelastic-loop.

3.3.4 Convergence of the aeroelastic-loop

The aeroelastic-loop iterates between aerodynamic loads and structural deflection computations until the wing tip vertical deformation δ_z does not change significantly between successive iterations k and $k-1$:

$$\left| \frac{\delta_z^k - \delta_z^{k-1}}{\delta_z^{k-1}} \right| < \varepsilon, \tag{3.8}$$

where ε is the relative tolerance. The default value of ε is set to 10^{-3}, and it can be adjusted by the user. A maximum number of 8 iterations is imposed to avoid an infinite loop in case of divergence of the results.

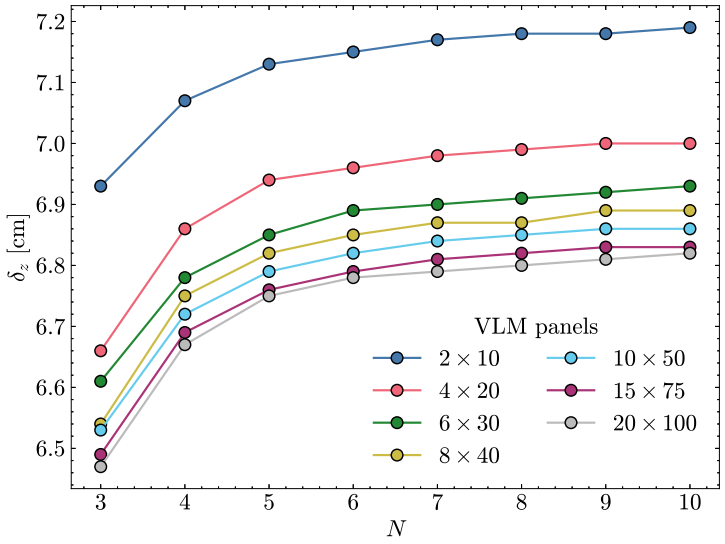

Figure 10 – Convergence of the mid-chord wing tip vertical deflection δ_z, as function of the number of structural nodes N. Each curve corresponds to a different VLM discretization of the wing into $N_{\text{chord}} \times N_{\text{span}}$ panels. Wing geometry and flow conditions: $b/2 = 5$ m, $t = 0.02$ m, $U_\infty = 30\ \text{m}\,\text{s}^{-1}$, $\alpha = 1°$.

4 Results and discussions

This section presents the results of the aeroelastic model developed in this work, AeroFrame. The model validation is performed in three main parts. First, AeroFrame results are compared with available data from the literature. Then, the model outputs are evaluated against medium- and high-fidelity computations. Finally, some aeroelastic computations are performed on real wing geometry and compared with high-fidelity calculations. The results section ends with an investigation of the effects of the sweep angle and the taper ratio on the structural response of a wing.

4.1 Model validation

4.1.1 Literature-based validation

The first validation tests are made using available results from the literature. The outputs of the newly developed model are compared with the results of V. Gulizzi and I. Benedetti [5], and E. Carrera et al. [2]. In both references, the VLM is coupled with a 1-dimensional FEM beam model. Additionally, E. Carrera et al. [2] provide deformation results computed using a NASTRAN shell model, again with the aerodynamic loads computed using VLM. The test case is a rectangular flat wing made of an isotropic homogeneous elastic material having an elastic modulus $E = 69$ GPa, and a shear modulus $G = 25.9$ GPa. The chord of the wing is $c = 1$ m, the free-stream air density ρ_∞ is set to $1.225\ \text{kg}\,\text{m}^{-3}$, and the angle of attack is $\alpha = 1°$ for all computations. The rectangular wing is discretized into 10×50 panels, while the beam mesh is composed of $N = 5$ nodes in all tests. The span of the full wing b, its thickness t, and the free-stream velocity U_∞ are varying throughout the tests.

Convergence analysis and verification of work conservation: Before making simulations to compare the results of the newly developed model with those from literature, a convergence study of the aeroelastic model is performed for a wing geometry with $b/2 = 5$ m and $t = 0.02$ m, a free-stream velocity $U_\infty = 30\ \text{m}\,\text{s}^{-1}$ and an angle of attack $\alpha = 1°$. For each discretization of

U_∞ [m/s]	W^A_{tot} [J]	W^S_{tot} [J]	Difference [%]
10	$1.306 \cdot 10^{-6}$	$1.323 \cdot 10^{-6}$	1.3
30	$1.732 \cdot 10^{-3}$	$1.745 \cdot 10^{-3}$	0.75
50	$5.513 \cdot 10^{-3}$	$5.537 \cdot 10^{-3}$	0.38

Table 1 – Verification of the work conservation principle between the total aerodynamic work W^A_{tot} and the total structural work W^S_{tot} at varying free-stream velocities. Wing geometry and flow conditions: $b/2 = 5$ m, $t = 0.02$ m, $\alpha = 1°$.

the wing surface into $N_{\text{chord}} \times N_{\text{span}}$ panels, the number of beam nodes N is increased from 3 to 10. This allows to observe the impact of both fluid and structural meshes on the convergence behavior. As can be seen from fig. 10, for each VLM discretization, the wing tip deflection δ_z converges to a stable value when N increases. While the VLM discretization is refined, the values of δ_z collapse into a single curve. This study shows that AeroFrame computations are consistent in term of convergence when the meshes are refined.

Additionally, a verification of the work conservation during the data transfer between the fluid and the structural meshes is done. Based on eqs. (3.5) and (3.6), and on the work conservation principle, the total aerodynamic work, expressed as

$$W^A_{\text{tot}} = \sum_{i=1}^{M} \boldsymbol{F}^A_i \cdot \boldsymbol{\delta}^A_i, \tag{4.1}$$

must be equal to the total structural work

$$W^S_{\text{tot}} = \sum_{j=1}^{N} \left(\boldsymbol{F}^S_j \cdot \boldsymbol{\delta}^S_j + \boldsymbol{M}^S_j \cdot \boldsymbol{\theta}^S_j \right), \tag{4.2}$$

where M and N are the number of VLM and beam nodes, respectively. A comparison of W^A_{tot} and W^S_{tot} is made for a wing geometry with $b/2 = 5$ m and $t = 0.02$ m at increasing free-stream velocities, with angle of attack $\alpha = 1°$. The values of W^A_{tot} and W^S_{tot}, reported in table 1, are very close to each other. The maximum variation between W^A_{tot} and W^S_{tot} is in the order of 1%. This confirms that the work is conserved during the aeroelastic-loop, and that forces and moments transferred to the beam nodes accurately reflect the original aerodynamic forces applied to the wing panels.

Varying free-stream velocity: The first tests are performed with a semi-span $b/2 = 5$ m, a thickness $t = 0.02$ m, at different free-stream velocities U_∞. D. Huixue et al. [21] found that for a deflection smaller than 1.62% of the semi-pan length, the nonlinear effects of the structural response are negligible. This criteria should be taken into account, as the beam model used in AeroFrame is linear. The values of the mid-chord tip deflection obtained from AeroFrame are in good agreement with those of the references (fig. 11a). A maximum relative variation of 8% with respect to the reference results is found in the linear region, for $U_\infty \leq 30$ m s^{-1} (white shaded area in fig. 11a). For a free-stream velocity $U_\infty = 50$ m s^{-1}, the results are more dispersed. AeroFrame δ_z value follows that of the beam model of ref. [2], but is 23% below the value obtained with the shell NASTRAN computation. At this free-stream velocity, the wing deformation reaches the nonlinear regime of the structural response (gray shaded area in fig. 11a). The use of a linear beam model that does not capture the geometric nonlinear effects can be an explanation for these disparities in the results.

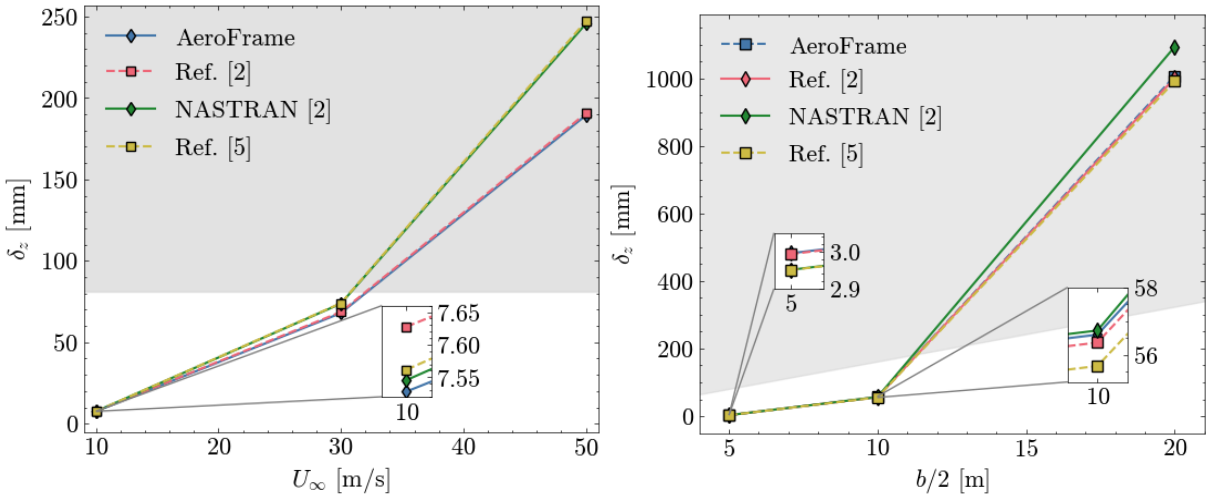

(a) (b)

Figure 11 – AeroFrame results for mid-chord wing tip vertical deflection δ_z, compared with the values from references [5] and [2]. The VLM mesh is composed of 10×50 panels, coupled with $N = 5$ beam nodes. The white shaded area represents the region of validity of the linear beam model, according to D. Huixue et al. [21]. (a) Influence of the free-stream velocity for a wing geometry with $b/2 = 5$ m, $t = 0.02$ m, and $\alpha = 1°$. (b) Influence of the wing semi-span $b/2$ for a wing thickness $t = 0.1$ m, with $U_\infty = 70\ \mathrm{m\,s^{-1}}$ and $\alpha = 1°$.

Varying wing span: The tests are made with a wing thickness of $t = 0.1$ m, a free-stream velocity of $U_\infty = 70\ \mathrm{m\,s^{-1}}$, for a varying wing span length. Once again the AeroFrame values of δ_z are in very good agreement with those of the literature, with a maximum relative variation of 1.7% in the linear structural regime for $b/2 \leq 10$ m (white shaded area in fig. 11b). A deviation from the NASTRAN shells results is observed for $b/2 = 20$ m in the nonlinear region, while the AeroFrame value follows those of the beam model of both references.

These first validation tests show that AeroFrame results are consistent with respect to literature data and are accurate in the linear regime of the structural response. When the wing deflection reaches the nonlinear region, the results need to be cautiously interpreted, and considered as a rough estimation of the deformation.

4.1.2 Comparison with medium- and high-fidelity computations

Additional validation tests are made by comparing AeroFrame results with medium-fidelity (Euler equations) and high-fidelity (Navier-Stokes equations) computations, both coupled with a shell model. A rectangular wing of thickness $t = 4.1$ mm, semi-span $b/2 = 1.6$ m, and chord length $c = 0.35$ m is used throughout the tests (fig. 12). The latter is made of isotropic material with an elastic modulus $E = 325$ GPa and a shear modulus $G = 125$ GPa. The free-stream air density is $\rho_\infty = 1.225\ \mathrm{kg\,m^{-3}}$. In AeroFrame, the VLM discretization is made of 20×100 panels and 50 beam nodes are employed for the structural mesh.

The CFD meshes are made during this study using `Ansys ICEM CFD`, then the steady CFD Euler and Navier-Stokes calculations are solved with the Navier-Stokes Multi-Block (`NSMB`) solver, using a central differencing space scheme. `NSMB` is coupled with a nonlinear shell model made of 10×50 elements, created with the `B2000++` CSM solver. The Spalart-Allmaras one-equation turbulence model and Sutherland law for viscosity are used in the Navier-Stokes calculations. The Fluid-Structure Connector (`FSCON`) spatial coupling tool is employed to couple the CFD and

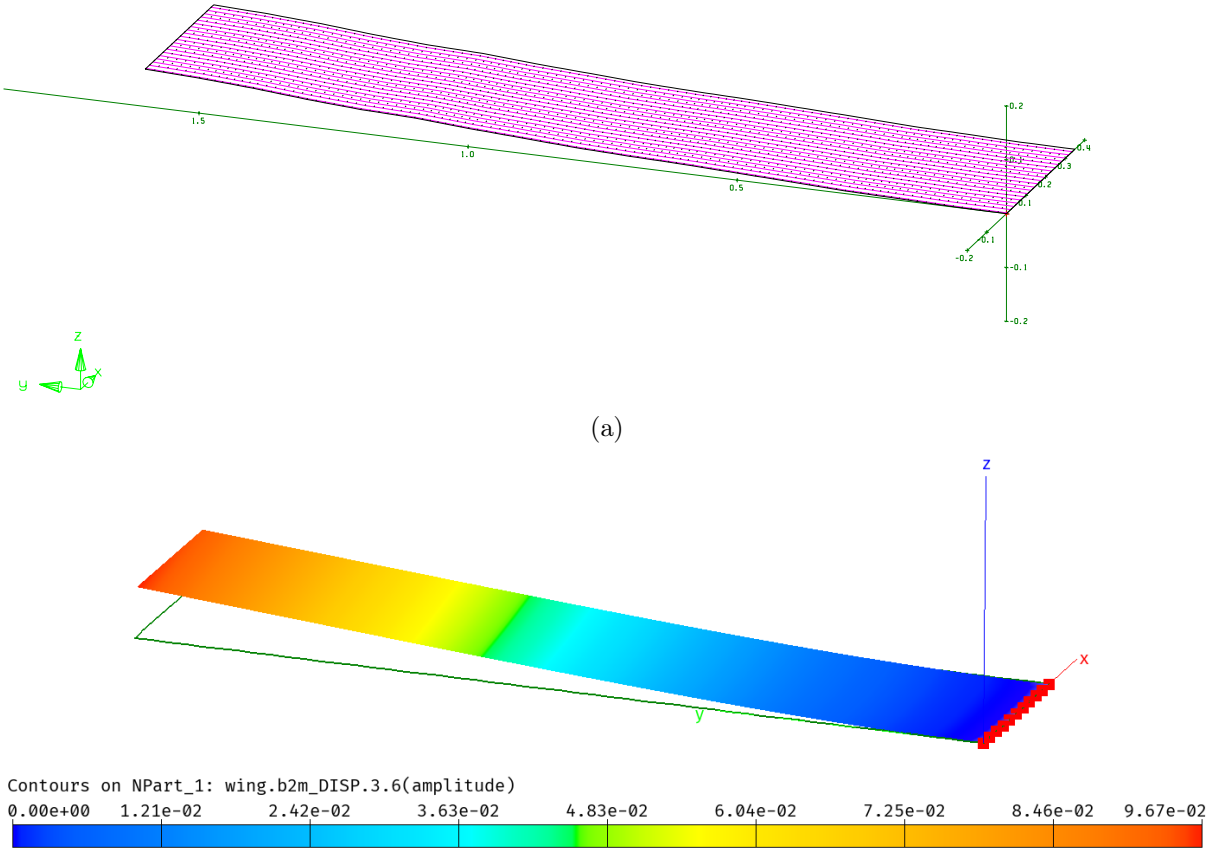

Figure 12 – Deformation of the rectangular wing obtained from (a) `AVL` and (b) `B2000++`. Wing geometry and material properties: $b/2 = 1.6$ m, $c = 0.35$ m, $t = 4.1$ mm, $E = 325$ GPa, $G = 125$ GPa. Flow conditions: $U_\infty = 50\ \mathrm{m\,s^{-1}}$, $\alpha = 1.5°$, $\rho_\infty = 1.225\ \mathrm{kg\,m^{-3}}$.

CSM databases. The aeroelastic calculations are performed as follows. First, 3000 CFD steps are made to compute the flow around the undeformed wing, and the resulting aerodynamic forces are interpolated on the structural mesh. The CSM model computes a first deformation, which is translated into a displacement of the nodes of the fluid mesh, leading to a new CFD grid used to get the updated flow solution. Between each structural deformation, 300 CFD steps are made to obtain the altered flow around the deformed wing configuration. This process iterates until the structural displacements converge.

Two flow configuration studies are made in this validation part. First, the angle of attack is increased at a constant free-stream velocity of 17 $\mathrm{m\,s^{-1}}$. Then, the angle of attack is maintained at $\alpha = 1.5°$ while the free-stream velocity is increasing from 2 to 50 $\mathrm{m\,s^{-1}}$.

Increasing angle of attack: For this flow configuration, only the Navier-Stokes computations are solved and compared with AeroFrame results. The Euler calculations encountered convergence issues within the first 3000 CFD steps for angles of attack $\alpha \geq 3°$. This problem is due to the wing's rectangular profile, which presents a sharp leading edge. As a result, flow separation occurs rapidly with increasing incidence, and the Euler calculations struggle to capture this phenomenon. In the linear deformation regime, AeroFrame results for tip deflection are close to those computed with high-fidelity methods, with a maximum relative variation of 10% (white-shaded area in fig. 13a). High-fidelity results show a larger slope of δ_z with respect to α up to an incidence of 6°. Beyond this angle of attack the slope decreases, illustrating the influence

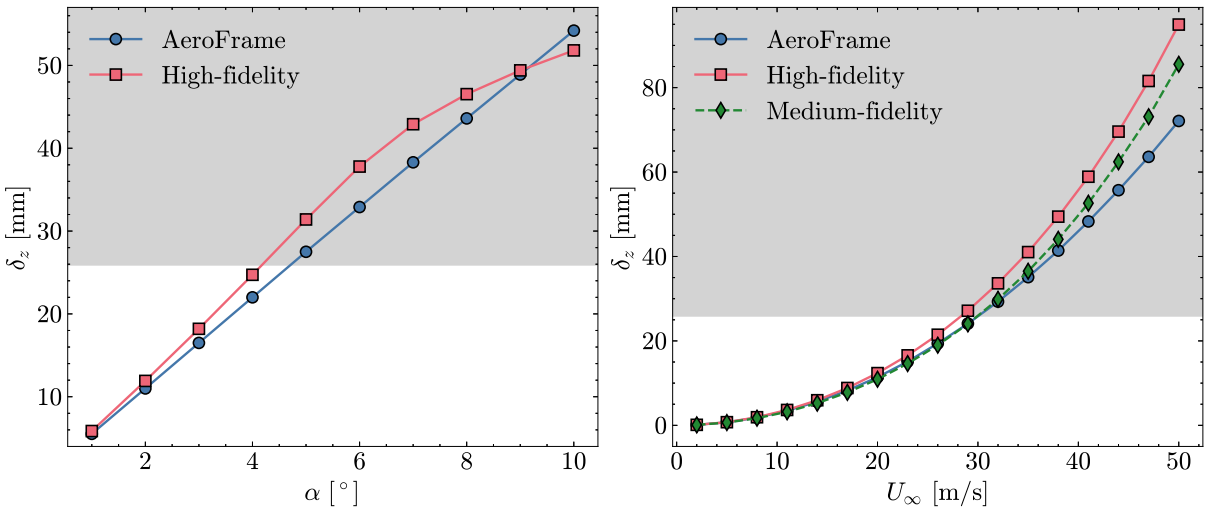

(a) (b)

Figure 13 – AeroFrame results for mid-chord wing tip vertical deflection δ_z, compared with medium- and high-fidelity computations (Euler/Navier-Stokes solution and nonlinear shell model with 10×50 elements). The VLM mesh is composed of 20×100 panels, coupled with $N = 50$ beam nodes. The white shaded area represents the region of validity of the linear model, according to D. Huixue et al. [21]. (*a*) Influence of the angle of attack at free-stream velocity $U_\infty = 17\ \mathrm{m\,s^{-1}}$. (*b*) Influence of the free-stream velocity for an angle of attack $\alpha = 1.5°$.

of flow separation on the variation of aerodynamic forces. AeroFrame, which uses the VLM to compute the flow, does not capture the occurrence of stall; consequently, the wing deflection keeps increasing linearly with the incidence angle.

Increasing free-stream velocity: For these calculations the angle of attack is maintained at $\alpha = 1.5°$, therefore no convergence issues are encountered for the Euler calculations. AeroFrame values of δ_z are in very good agreement with those obtained from the coupling of `NSMB` and `B2000++` in the linear region of the structural response (fig. 13b). A mean relative variation of 5.6% and 6.8% is found with respect to medium- and high-fidelity results. For $U_\infty > 30\ \mathrm{m\,s^{-1}}$, larger deformations are obtained and the three curves start to differ. This shows that in the small deformation regime, both the linear beam model and the nonlinear shell model yield similar δ_z values. When the wing deflection is larger than about 2% of the semi-span length, the geometric nonlinearity becomes important and the small displacements approximation is no longer valid. In this deformation regime, the linear beam model of AeroFrame underestimates the wing tip deflection, and deviates from the nonlinear shell model that captures large deformations and rotations.

The fact that both medium- and high-fidelity calculations employ the same structural model allows the observation the impact of the type of CFD simulations used. AeroFrame results are closer to those obtained from Euler equations because the assumptions of the VLM, such as inviscid flow, align more closely with the Euler equations than with the Navier-Stokes equations. The latter account for viscous forces and turbulence, resulting in aerodynamic forces that differ from those predicted by potential flow theory or the Euler equations.

The validation tests confirm that the wing deflection is accurately captured in the small displacement region, for different flow conditions. But AeroFrame, using a linear beam model, underestimates the deformation when nonlinear effects become significant.

Scaling analysis: AeroFrame results show a linear relation between δ_z and α when the free-stream velocity is constant (fig. 13a), and a quadratic increase of δ_z with respect to U_∞ when the incidence is constant (fig. 13b). This can be explained using basic aerodynamic scaling arguments. Generally, the lift force L is expressed as

$$L = \frac{1}{2}\rho_\infty U_\infty^2 S C_L, \tag{4.3}$$

where C_L is the lift coefficient, S is the wing surface area, and ρ_∞ is the free-stream density. For thin lifting surface with small incidence, the lift coefficient C_L is proportional to the angle of attack α. Hence, if the fluid flow is incompressible, it follows that

$$L \sim U_\infty^2 \alpha. \tag{4.4}$$

In the small displacements approximation, the deflection depends linearly on the applied force, i.e $\delta_z \sim L$. Combining this scaling with eq. (4.4) leads to:

$$\delta_z \sim U_\infty^2 \alpha. \tag{4.5}$$

This confirms that for a constant free-stream velocity, $\delta_z \sim \alpha$, and for a constant incidence, $\delta_z \sim U_\infty^2$. These results show that AeroFrame captures the fundamental relations derived from potential flow theory and linear beam theory.

4.2 Results for aircraft wing geometry

The initial validation of AeroFrame was made using a simple rectangular wing configuration. In this section, results of aeroelastic computations using a more complex wing geometry are discussed. The latter, the MDO wing, features multiple sections with varying sweep and dihedral angles, as well as a changing airfoil profile along the span. It was developed and analyzed in the

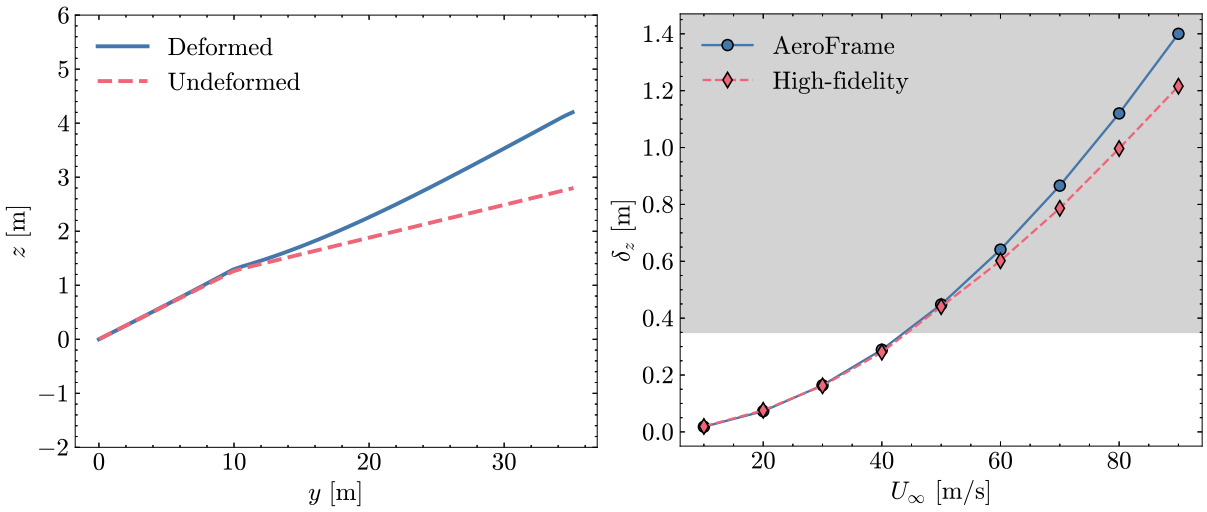

(a) (b)

Figure 14 – Analysis of the MDO wing for $\alpha = 4°$, $\rho_\infty = 1.1116\ \mathrm{kg\,m^{-3}}$ and a discretization of 20×100 panels coupled with $N = 75$ beam nodes. (a) Final deformation along the span for $U_\infty = 90\ \mathrm{m\,s^{-1}}$, compared to the undeformed shape in the $y-z$ plane (note that both axes have different scales). (b) Wing tip vertical deflection as function of the free-stream velocity. The white shaded area represents the region of validity of the linear model, according to D. Huixue et al. [21].

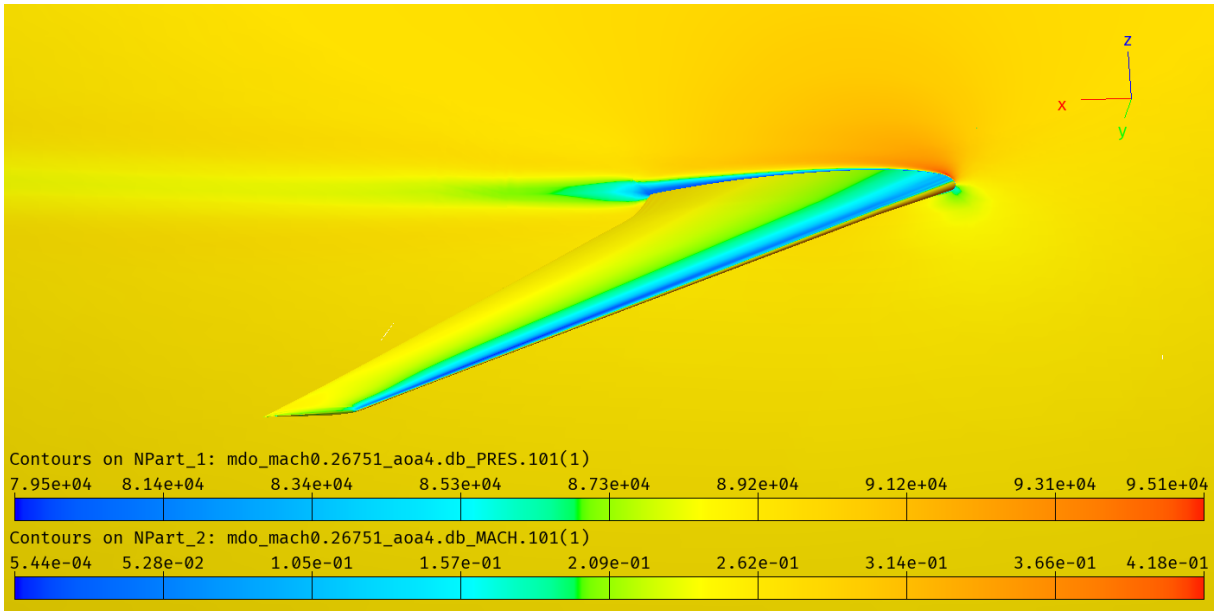

(a)

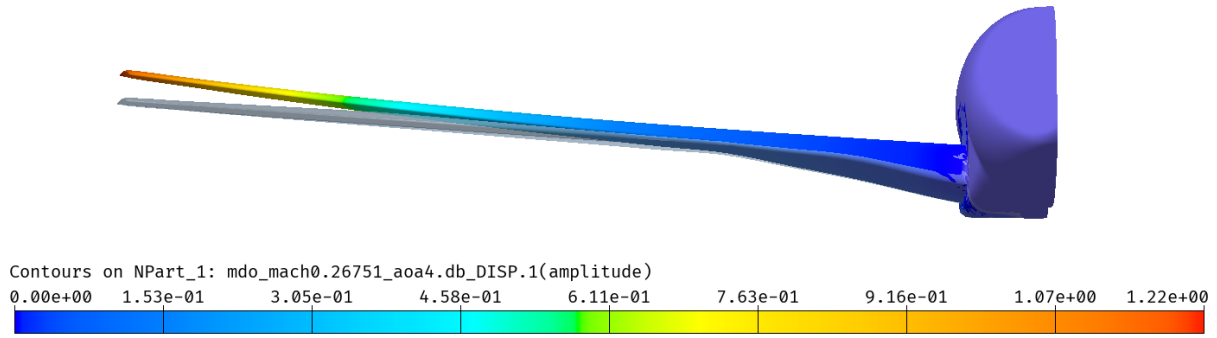

(b)

Figure 15 – CFD and CSM results for the MDO wing at $\alpha = 4°$, $U_\infty = 90\ \mathrm{m\,s^{-1}}$, $\rho_\infty = 1.1116\ \mathrm{kg\,m^{-3}}$. (a) Flow solution around the undeformed wing: pressure distribution on the wing surface, and Mach number contour on a cut in a streamwise plane along the span.
(b) Deflection of the wing along the span, the undeformed configuration is shown in gray.

UNSI (Unsteady Viscous Flow in the Context of Fluid-Structure Interaction) European funded project, which involved performing steady-state transonic aeroelastic computations [24]. As a consequence, the CFD and the CSM meshes were already available. The MDO wing has a semi-span length $b/2 = 35$ m, an elastic modulus $E = 71$ GPa, and a shear modulus $G = 27$ GPa. A discretization of 20×100 VLM panels is coupled with $N = 75$ beam nodes. In addition to AeroFrame results, high-fidelity computations are done using `NSMB` and `B2000++` solvers. The steady, compressible, Navier-Stokes equations are solved using the Spalart-Allmaras turbulence model and the Sutherland viscosity law. The approach is similar to the one used in section 4.1.2. The flow solution around the undeformed wing configuration is obtained after 5000 CFD steps (fig. 15a). Then, a first deformation is computed by the nonlinear CSM beam model, and a new CFD grid is generated. The process continues with 500 CFD steps, followed by a new deformation, and repeats until convergence is achieved (fig. 15b). The wing tip deflection is computed for an angle of attack $\alpha = 4°$, with an increasing free-stream velocity from 10 to $90\ \mathrm{m\,s^{-1}}$. The flight altitude is set to 1 km, resulting in a free-stream density $\rho_\infty = 1.1116\ \mathrm{kg\,m^{-3}}$.

The values of the wing tip deflection δ_z computed with AeroFrame and high-fidelity methods

are very close for $U_\infty \leq 50$ m s^{-1} (fig. 14b), with a mean relative difference of 3.1%. The results differ by 6% to 15% for higher free-stream velocities, when the large deformation regime is reached. This result confirms that AeroFrame can solve linear aeroelastic problems for a complex aircraft wing geometry. Figure 14a shows the final shape of the wing along the span, as well as the undeformed configuration. In the wing root proximity, the deflection is close to zero for $y \leq 10$ m, i.e. both deformed and undeformed shapes are similar. In this region of the span, the surface and the second moments of area of the cross-section are high, resulting in a strong bending rigidity and a small deformation under the lift loading. For $y > 10$ m, an increase of the deflection is observed due to the reduction of the wing cross-section. This shows an example of the structural response of a wing with variable geometric properties along the span.

4.3 Effect of sweep angle and taper ratio on wing deflection

The validation tests have shown that AeroFrame results are consistent with literature data and medium- to high-fidelity computations. This section investigates the influence of the sweep angle Λ and the taper ratio $\lambda = c_t/c_r$ on the structural response of a wing with a NACA 0012 airfoil profile. The semi-span is $b/2 = 6$ m and the root chord length is $c_r = 1$ m (fig. 16, left). The taper ratio varies between 0.2 and 0.8, while the sweep angle ranges from $-10°$ to $20°$. The elastic and shear moduli of the wing material are $E = 40$ GPa and $G = 15$ GPa, respectively. The wing is discretized into 20×100 panels, which are coupled with 75 beam nodes.

For every combination of Λ and λ, the wing tip deflection δ_z and the wing tip twist angle θ_y are computed (fig. 17) under constant flow conditions: $\alpha = 3°$, $U_\infty = 68$ m s^{-1}, and $\rho_\infty = 1.225$ kg m^{-3}. The minimum wing tip deflection is found for a sweep angle of $5°$ for all values of taper ratio. Furthermore, for a given sweep angle Λ, the deflection increases with the taper ratio. Indeed, the value of λ directly affects the lift distribution generated along the wing span; a low taper ratio tends to change the distribution towards an elliptical one, which moves the center of pressure inboard to the fuselage axis. This reduces the bending moment applied at the wing root and decreases the tip deflection [26].

The tip twist angle θ_y decreases linearly with the sweep angle; for $\Lambda > 2°$, θ_y becomes negative and increases as the taper ratio is decreased. Negative sweep angles result in a positive twist, indicating that swept-forward wings are more sensitive to divergence. Indeed, this positive twist

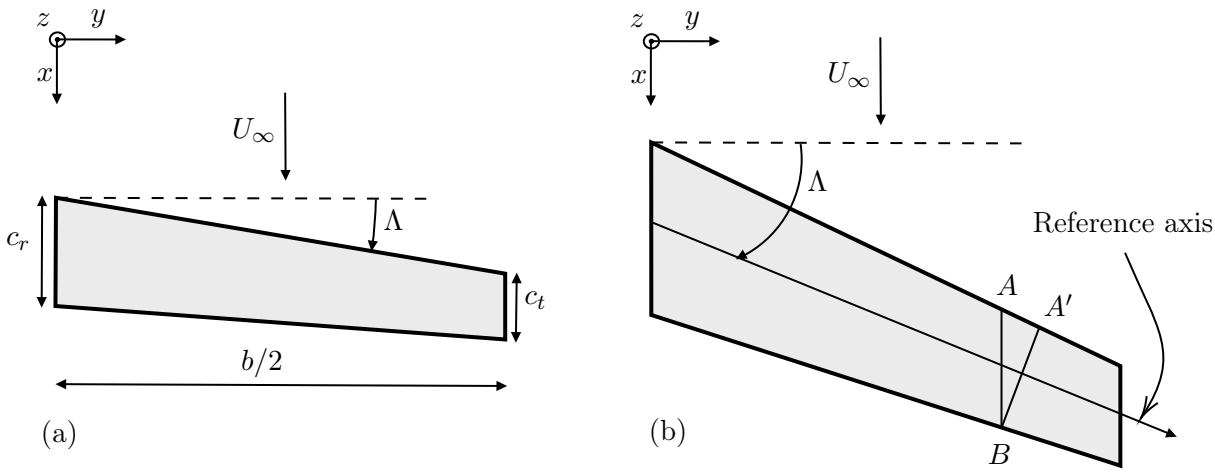

Figure 16 – (a) Wing geometry used to investigate the effect of the sweep angle Λ and the taper ratio $\lambda = c_t/c_r$. Wing dimensions and material properties: $b/2 = 6$ m, $c_r = 1$ m, $E = 40$ GPa, $G = 15$ GPa. (b) Effect of the sweep angle Λ on the displacement of streamwise segment AB and segment $A'B$ perpendicular to the reference axis of the wing (figure adapted from [8, 25]).

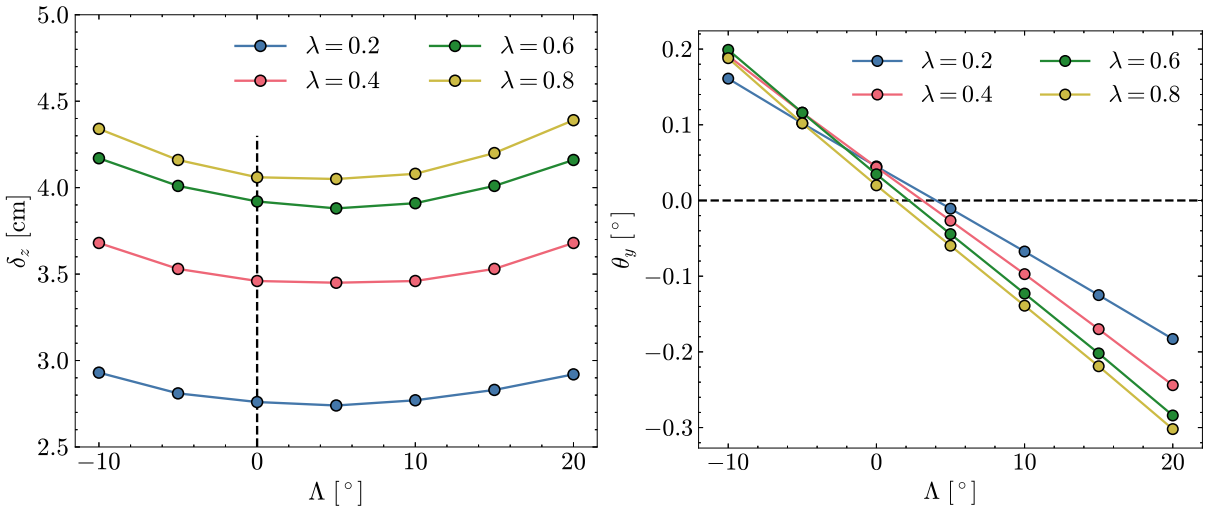

Figure 17 – Effect of sweep angle Λ and taper ratio $\lambda = c_t/c_r$ on (a) the wing tip deflection δ_z and (b) the tip twist θ_y. Flow conditions: $\alpha = 3°$, $U_\infty = 68\ \mathrm{m\,s^{-1}}$, $\rho_\infty = 1.225\ \mathrm{kg\,m^{-3}}$. Discretization: 20×100 panels and $N = 75$ beam nodes.

increases the incidence of the wing, leading to higher aerodynamic loads and greater deformation. In contrast, positively swept wings exhibit negative twist angles, making them statistically stable. This phenomenon is due to the orientation of the reference axis of the wing, which is no longer perpendicular to the free-stream direction in the case of a swept-wing. Consider the swept-backward wing in fig. 16 (right); segment AB is in the streamwise direction while segment $A'B$ is perpendicular to the reference axis. Due to the lift distribution applied on the reference axis, points A' and B are deflected by approximately the same distance [25]. The latter distance being greater than the displacement of point A, the incidence of the streamwise segment AB is decreased, leading to a diminution of the lift force. This configuration is therefore stable; this explains why swept-backward wings exhibit very high divergence speed, or sometimes never diverge [27]. The converse holds for swept-forward wings; the vertical deflection of the wing due to bending leads to an increase of the incidence of the streamwise sections, resulting in a positive increment of lift force and a greater incidence. In this case, bending deflections contribute to static instability, resulting in very low divergence speeds [8].

5 Limitations and prospects for improvement

Despite the effectiveness of the current methodology, the numerical aeroelastic tool developed in this work faces limitations, and multiple aspects can be enhanced. Alternative interpolation techniques, such as radial basis functions or weighted residual methods, could provide more accurate mapping of the loads and the displacements between fluid and structural meshes, and improve the overall robustness [28, 7]. The integration of a nonlinear beam model would allow for more accurate capture of large displacements and rotations occurring at high free-stream velocities and high incidence. The possibility to use anisotropic composite materials could represent a significant improvement, giving the opportunity to define distinct values for elastic modulus and Poisson's ratio in the transverse and longitudinal directions of the fibers. These materials are widely used in wing manufacturing, as they enhance efficiency by combining good mechanical properties with reduced weight. Another improvement of the present aeroelastic tool would be to integrate wing control surfaces, such as flaps or ailerons. The vortex lattice method solver

AVL allows the use of control surfaces, but the aircraft geometry definition in CPACS format does not deal with them yet. Finally, it is important to keep in mind that the present numerical tool is to be used for conceptual aircraft design; the calculation time should stay reasonably small in order to be able to rapidly make a large amount of analysis. A trade-off needs to be made between improving the model and not increasing the computational cost.

6 Conclusion

The vortex lattice method has been coupled with a finite element method implementation of the linear Euler-Bernoulli beam equations to create a low-fidelity aeroelastic module, called AeroFrame, in the open source conceptual aircraft design environment CEASIOMpy. A partitioned approach has been used, i.e. separate numerical solvers were employed for fluid and structural computations: AVL and FramAT, respectively. The mapping of aerodynamic forces and structural displacement between the two non-matching meshes has been done with the nearest neighbor interpolation method. To ensure the aeroelastic-loop is physically meaningful, all aerodynamic loads were transmitted from the fluid to the structure, and the work done by the fluid on the panel surface was imposed to be the same as the work done by the transferred forces on the structure.

A convergence analysis of the tip deflection of a rectangular wing has shown that AeroFrame results are consistent when both fluid and structural meshes are refined. In the region of linear deformation behavior, the results of the developed aeroelastic tool are in good agreement with literature data and medium- to high-fidelity computations. The validation tests were conclusive for simple rectangular wings, as well as for a complex aircraft wing geometry with variable cross-section, sweep angle, and dihedral angle. For large displacements, AeroFrame results differ from nonlinear solutions obtained from shell models and cannot be considered accurate. In a last part, the effect of the sweep angle and the taper ratio on the wing deformation was investigated, showing an increase of the tip deflection with the taper ratio. It was found that for any value of the taper ratio, there exists an optimal sweep angle that minimizes the wing deflection. Swept-forward wings, resulting in a positive twist due to bending deformation, were found to be sensitive to divergence. In contrast, a negative twist was computed for swept-backward wings, showing a statically stable behavior.

The AeroFrame module is well-suited for preliminary aircraft design tasks, demonstrating high accuracy in small deformation scenarios and providing rough estimations when the large displacement regime is reached. Its low computational cost enables extensive analyses, facilitating iterative analyses across various material properties and wing geometries. The computational time required by AeroFrame is in the order of minutes, which is significantly faster than high-fidelity methods, requiring several hours to produce results.

References

[1] M. Bras, S. Warwick, and A. Suleman, "Aeroelastic evaluation of a flexible high aspect ratio wing UAV: Numerical simulation and experimental flight validation," *Aerospace Science and Technology*, vol. 122, p. 107400, Mar. 2022.

[2] E. Carrera, A. Varello, and L. Demasi, "A refined structural model for static aeroelastic response and divergence of metallic and composite wings," *CEAS Aeronautical Journal*, vol. 4, pp. 175–189, June 2013.

[3] A. Aşkan and S. Tangöz, "The effect of aspect ratio on aerodynamic performance and flow separation behavior of a model wing composed from different profiles," July 2018.

[4] J. D. Anderson, *Fundamentals of Aerodynamics*. New York, NY: McGraw Hill, 6th edition ed., Mar. 2016.

[5] V. Gulizzi and I. Benedetti, "Computational aeroelastic analysis of wings based on the structural discontinuous Galerkin and aerodynamic vortex lattice methods," *Aerospace Science and Technology*, vol. 144, p. 108808, Jan. 2024.

[6] M. Alder, E. Moerland, J. Jepsen, and B. Nagel, "Recent Advances in Establishing a Common Language for Aircraft Design with CPACS," (Bordeaux, Frankreich), 2020.

[7] K. Li, J. Kou, and W. Zhang, "Aeroelastic reduced-order modeling for efficient static aeroelastic analysis considering geometric nonlinearity," *Journal of Fluids and Structures*, vol. 124, p. 104055, Jan. 2024.

[8] T. Megson, *Aircraft Structures for Engineering Students*. Aug. 2021.

[9] M. Drela, "Flight Vehicle Aerodynamics," Feb. 2014.

[10] J. Katz and A. Plotkin, *Low-Speed Aerodynamics*. Cambridge Aerospace Series, Cambridge: Cambridge University Press, 2 ed., 2001.

[11] J. J. Bertin and M. L. Smith, *Aerodynamics for Engineers*. Prentice-Hall, 1979. Google-Books-ID: gKFTAAAAMAAJ.

[12] A. Dettmann, *Loosely coupled, modular framework for linear static aeroelastic analyses*. 2019.

[13] M. Luo, Z. Wu, and C. Yang, "Strongly coupled fluid–structure interaction analysis of aquatic flapping wings based on flexible multibody dynamics and the modified unsteady vortex lattice method," *Ocean Engineering*, vol. 281, p. 114921, Aug. 2023.

[14] F. Dorbath, B. Nagel, and V. Gollnick, "Comparison of Beam and Shell Theory for Mass Estimation in Preliminary Wing Design," Oct. 2010.

[15] O. A. Bauchau, J. I. Craig, and G. M. L. Gladwell, eds., *Structural Analysis*, vol. 163 of *Solid Mechanics and Its Applications*. Dordrecht: Springer Netherlands, 2009.

[16] L. Andersen and S. R. Nielsen, "Elastic Beams in Three Dimensions," Aug. 2008.

[17] "DLR-SC/tixi," May 2024. original-date: 2015-03-16T13:17:12Z.

[18] A. Dettmann, "ambiance: A full implementation of the ICAO standard atmosphere 1993."

[19] "airinnova/framat," May 2024. original-date: 2019-08-13T13:15:55Z.

[20] A. Rizzi and J. Oppelstrup, *Aircraft Aerodynamic Design with Computational Software*. Cambridge: Cambridge University Press, 2021.

[21] H. Dang, Z. Yang, and Y. Li, "Accelerated loosely-coupled CFD/CSD method for nonlinear static aeroelasticity analysis," *Aerospace Science and Technology*, vol. 14, pp. 250–258, June 2010.

[22] A. de Boer, A. H. van Zuijlen, and H. Bijl, "Review of coupling methods for non-matching meshes," *Computer Methods in Applied Mechanics and Engineering*, vol. 196, pp. 1515–1525, Jan. 2007.

[23] A. Kafkas and G. Lampeas, "Static Aeroelasticity Using High Fidelity Aerodynamics in a Staggered Coupled and ROM Scheme," *Aerospace*, vol. 7, p. 164, Nov. 2020. Number: 11 Publisher: Multidisciplinary Digital Publishing Institute.

[24] W. Haase, V. Selmin, and B. Winzell, "Progress in Computational Flow-Structure Interaction. Results of the Project UNSI, supported by the European Union 1998 – 2000," pp. 289–304, Jan. 2003.

[25] R. L. Bisplinghoff, H. Ashley, and R. L. Halfman, *Aeroelasticity*. Courier Corporation, Jan. 1996. Google-Books-ID: jtqDQ2nTvvcC.

[26] R. S. Shevell, *Fundamentals of Flight*. Englewood Cliffs, N.J: Pearson, 2nd edition ed., Aug. 1988.

[27] F. W. Diederich and B. Budiansky, "Divergence of swept wings," Aug. 1948. NTRS Author Affiliations: NTRS Report/Patent Number: NACA-TN-1680 NTRS Document ID: 19930082318 NTRS Research Center: Legacy CDMS (CDMS).

[28] R. Maierl, A. Gastaldi, J.-N. Walther, and A. Jungo, "Aero-structural Optimization of a MALE Configuration in the AGILE MDO Framework," pp. 169–187, Jan. 2020.